On the Comparison between Population Balance Models for CFD Simulation of Bubble Columns

Jay Sanyal,[†] Daniele L. Marchisio,[*,‡] Rodney O. Fox,[‡] and Kumar Dhanasekharan[†]

Fluent Inc., Centerra Resource Park, 10 Cavendish Court, Lebanon, New Hampshire 03766-1442, and Department of Chemical Engineering, Iowa State University, 2114 Sweeney Hall, Ames, Iowa 50011-2230

CFD simulations of bubble columns have received much attention, and several multiphase models have been developed, tested, and validated through comparison with experimental data. It is well-known that bubble coalescence and breakup can lead to significant variations in the bubble size distribution and that, to model the evolution of the dispersed gas phase, the population balance equation has to be solved. In this work, a classes method (CM) and a method of moments (MOM) are investigated and compared. The MOM represents an attractive alternative in which, instead of tracking the entire bubble distribution, only the lower-order moments of the distribution are tracked. The above two approaches have been implemented in the commercial CFD code FLUENT, version 6.0, in conjunction with the Eulerian multiphase model.

1. Introduction

Bubble columns are widely used in industrial chemical processes because of their capability of achieving high heat- and mass-transfer rates with low energy input. The correct estimation of gas hold-up and superficial area are crucial in the design and optimization of these reactors. Because of its predictive capabilities, computational fluid dynamics (CFD) is rapidly becoming an important tool for these calculations. Yet, owing to the inherent complexity of the physical problem, use of CFD in modeling bubble columns has been limited compared to that in single-phase or dilute multiphase systems.

Recently, significant research efforts have been directed toward developing closure models for interfacial bubble−liquid forces[1] and estimating bubble-induced turbulence,[2] whereas little attention has been focused on the bubble size distribution problem. At low gas velocity and low gas hold-up, bubbles have roughly the same size, which is equal to the initial size at the inlet. However, at higher values of gas hold-up and velocity, because of coalescence and breakup, the bubble size distribution changes.

To account for the effect of hydrodynamics on the bubble size distribution, the conservation equations governing multiphase fluid flow need to be solved along with the population balance equation for the number density of bubbles. The two principal approaches that are frequently used to solve the fluid flow problem are the Eulerian−Lagrangian and the Eulerian−Eulerian methods. Whereas the former gives a direct physical interpretation of the fluid−bubble interaction, it becomes impractical to use for high volume fractions of the gas phase. This limitation is overcome in the latter method, where the gas and liquid phases are modeled as interpenetrating continuua and the continuity and momentum equations are solved for each phase separately.[3,4] A detailed discussion of the relative merits of the two methods can be found in ref 5. A comparison with experimental data and discussion of the numerical issues involved can be found in refs 6 and 7.

To model the rise characteristics of bubbles of different sizes, Van Baten and Krishna[8,9] assumed two different bubble classes (i.e., "small" and "large"). However, in this model, the interaction between the two classes in terms of coalescence and breakup was not taken into consideration. Lehr, Millies, and Mewes[10] modeled the population balance equations by writing a single transport equation for the average bubble volume that incorporated bubble coalescence and breakage. Although the description was limited to two bubble classes, their approach is notable because the evolution of the bubble size distribution had not been adequately addressed in the preceding literature.

Recently, the general formulation of the problem has been discussed, and a new approach, the direct quadrature method of moments (DQMOM), has been formulated and applied.[11] A natural alternative to the DQMOM is the classes method (CM) in which the bubble distribution is represented through a finite number of bubble classes and coalescence and breakup rates are transformed into birth and death rates for each class. The main advantage of the CM is that the bubble size distribution is directly known, whereas in the DQMOM, and in general in any method of moments (MOM), only the moments of the bubble size distribution are tracked.

In this work, the CM and MOM approaches are implemented in a commercial CFD code (FLUENT) and compared. In the CM, the population balance equations are solved in terms of the volume fractions of each bubble class. In the MOM, the population balance equations are represented in terms of transport equations of the moments of the bubble distribution. The momentum equations for the primary liquid phase and the dispersed gas phase are solved in conjunction with the respective continuity equations, and the moments are all advected by the gas-phase momentum flux.[12] Comparisons are carried out for different inlet conditions, and the relative advantages and disadvantages

* To whom correspondence should be addressed. E-mail: daniele.marchisio@polito.it. Fax: +39-011-5644699. Current affiliation: Dip. Scienza Materiali ed Ingegneria Chimica, Politecnico di Torino, C.so Duca degli Abruzzi 24, 10129 Torino, Italy.

[†] Fluent Inc.

[‡] Iowa State University.

10.1021/ie049555j CCC: $30.25
Published on Web 09/29/2004

of the two methods are discussed. It should be noted here that all of the simulations were performed for a two-dimensional, axisymmetric bubble column. In reality, this approach neglects the azimuthal component of the flow and, hence, is not truly reflective of the three-dimensional nature of such flows. Further, any CFD simulation requires that issues relating to grid independence and the effect of alternate turbulence models be investigated thoroughly. However, the main focus of this work is to investigate alternate approaches for solving the population balance equations in the context of multiphase flows and not the detailed modeling of the hydrodynamics in a bubble column reactor. Hence, in the interest of computational time and effort, the above issues are not discussed here. Finally, the possibility of implementing the two approaches with more sophisticated multiphase models is discussed.

2. Governing Equations

In this work, the Eulerian−Eulerian approach is used, and the conservation equations are solved for each phase in the Eulerian frame. The continuity equation for the liquid phase is:

$$\frac{\partial}{\partial t}(\alpha_l \rho_l) + \nabla\cdot(\alpha_l \rho_l \vec{v}_l) = 0 \tag{1}$$

where α_l is the liquid volume fraction, ρ_l is the density, and $\vec{v}_l$ is the velocity of the liquid phase. A similar equation is solved for the volume fraction of the gas phase, α_g. It is important to mention here that, in this work, only two phases are considered: one liquid phase and one gas phase. The momentum balance for the liquid phase is

$$\frac{\partial}{\partial t}(\alpha_l \rho_l \vec{v}_l) + \nabla\cdot(\alpha_l \rho_l \vec{v}_l \vec{v}_l) = -\alpha_l \nabla p + \nabla\cdot\tau_l + \vec{F}_{lg} + \alpha_l \rho_l (\vec{F}_l + \vec{F}_{lift,l} + \vec{F}_{vm,l}) \tag{2}$$

where τ_l is the stress−strain tensor for the liquid phase, $\vec{F}_l$ is an external body force, $\vec{F}_{lift,l}$ is a lift force, $\vec{F}_{vm,l}$ is the virtual mass force, and p is the pressure shared by all phases. An analogous equation is solved for the gas phase. The interaction force between phases depends on friction, pressure, cohesion, and other effects and can be described using the expression

$$\vec{F}_{lg} = K_{lg}(\vec{v}_g - \vec{v}_l) \tag{3}$$

where K_{lg} is the interphase momentum exchange coefficient, which is usually calculated as

$$K_{lg} = \frac{\alpha_l \rho_l f}{\tau_p} \tag{4}$$

where f is the drag coefficient and τ_p is the so-called relaxation time. The lift forces are mainly due to velocity gradients in the primary-phase flow field, whereas the virtual mass force is caused by the acceleration of one phase relative to the other. The virtual mass effect is significant when the secondary-phase density is much smaller than the primary phase density.

The drag coefficient in Fluent is based on the model of Schiller and Naumann.[13] The drag function f is given by

$$f = \frac{C_D Re}{24} \tag{5}$$

where

$$C_D = \begin{cases} 24(1 + 0.15Re^{0.687})/Re & Re \le 1000 \\ 0.44 & Re > 1000 \end{cases} \tag{6}$$

and Re is the relative Reynolds number defined as

$$Re = \frac{\rho_l |\vec{v}_g - \vec{v}_l| d_g}{\mu_l} \tag{7}$$

Turbulence could be included in the model by using the mixture turbulence model, which is an extension of the single-phase $k-\epsilon$ model, with additional terms for multiphase flows. The k and ϵ equations describing this model are written as

$$\frac{\partial}{\partial t}(\rho_m k) + \nabla\cdot(\rho_m \vec{v}_m k) = \nabla\cdot\left(\frac{\mu_{t,m}}{\sigma_k}\nabla k\right) + G_{k,m} - \rho_m \epsilon \tag{8}$$

and

$$\frac{\partial}{\partial t}(\rho_m \epsilon) + \nabla\cdot(\rho_m \vec{v}_m \epsilon) = \nabla\cdot\left(\frac{\mu_{t,m}}{\sigma_\epsilon}\nabla\epsilon\right) + \frac{\epsilon}{k}(C_{1\epsilon} G_{k,m} - C_{2\epsilon}\rho_m \epsilon) \tag{9}$$

where the mixture density and velocity, ρ_m and $\vec{v}_m$, respectively, are computed as

$$\rho_m = \sum_{i=1}^{N} \alpha_i \rho_i \tag{10}$$

and

$$\vec{v}_m = \frac{\sum_{i=1}^{N} \alpha_i \rho_i \vec{v}_i}{\sum_{i=1}^{N} \alpha_i \rho_i} \tag{11}$$

The turbulent viscosity is computed from

$$\mu_{t,m} = \rho_m C_\mu \frac{k^2}{\epsilon} \tag{12}$$

and the production of turbulence kinetic energy, $G_{k,m}$, is computed as

$$G_{k,m} = \mu_{t,m}(\nabla\vec{v}_m + (\nabla\vec{v}_m)^T) : \nabla\vec{v}_m \tag{13}$$

The details of this approach are described in the Fluent User Manual.[14]

2.1. Population Balance Model. Consider the continuity equation for the gas phase. If there is no mass transfer, the equation can be written as

$$\frac{\partial}{\partial t}(\alpha_g \rho_g) + \nabla(\alpha_g \rho_g \vec{v}_g) = 0 \tag{14}$$

Assuming the gas phase to be composed of spherical bubbles of diameter L, the secondary-phase volume fraction can be written as

$$\alpha_g(\mathbf{x},t) = \int_0^\infty n(L;\mathbf{x},t)\,\frac{\pi}{6}L^3\,\mathrm{d}L \tag{15}$$

where $n(L;\mathbf{x},t)$ is the bubble size distribution function. It is important to note that, usually, L is referred to as an internal coordinate in contrast to $\mathbf{x}$ and t, which are external coordinates. Equation 14 can be derived by integration of the bubble size variable L from the general population balance equation

$$\frac{\partial}{\partial t}[\rho_g n(L;\mathbf{x},t)] + \nabla\cdot[\rho_g n(L;\mathbf{x},t)\vec{v}_g)] = \rho_g S(L;\mathbf{x},t) \tag{16}$$

and its validity is limited to the case of constant gas density (i.e., incompressible gas). The source terms represent changes in the bubble size distribution due to coalescence and breakup and can be written as[12]

$$S(L;\mathbf{x},t) = B^c(L;\mathbf{x},t) - D^c(L;\mathbf{x},t) + B^b(L;\mathbf{x},t) - D^b(L;\mathbf{x},t) \tag{17}$$

where

$$B^c(L;\mathbf{x},t) = \frac{L^2}{2}\int_0^L \frac{\beta((L^3-\lambda^3)^{1/3},\lambda)}{(L^3-\lambda^3)^{2/3}} n((L^3-\lambda^3)^{1/3};\mathbf{x},t)\,n(\lambda;\mathbf{x},t)\,\mathrm{d}\lambda \tag{18}$$

$$D^c(L;\mathbf{x},t) = n(L;\mathbf{x},t)\int_0^\infty \beta(L,\lambda)\,n(\lambda;\mathbf{x},t)\,\mathrm{d}\lambda \tag{19}$$

$$B^b(L;\mathbf{x},t) = \int_L^\infty a(\lambda)\,b(L|\lambda)\,n(\lambda;\mathbf{x},t)\,\mathrm{d}\lambda \tag{20}$$

$$D^b(L;\mathbf{x},t) = a(L)n(L;\mathbf{x},t) \tag{21}$$

In these expressions, B^c and D^c are the birth and death terms due to coalescence, B^b and D^b are the birth and death terms due to breakup, $\beta(L,\lambda)$ is the coalescence kernel, $a(L)$ is the breakup kernel, and $b(L|\lambda)$ is the daughter distribution function. We will return later to the specific forms of these terms.

The mean bubble size of the distribution is usually determined according to

$$d_{32}(\mathbf{x},t) = \frac{\int_0^\infty n(L;\mathbf{x},t)L^3\,\mathrm{d}L}{\int_0^\infty n(L;\mathbf{x},t)L^2\,\mathrm{d}L} \tag{22}$$

which can be thought of as the ratio between the total bubble volume and total bubble surface. The population balance equation for the secondary phase has to be solved within the CFD code. In fact, according to the functional form of $S(L;\mathbf{x},t)$, the distribution is altered, and thus $d_{32}(\mathbf{x},t)$ is also modified accordingly. The change in $d_{32}(\mathbf{x},t)$ produces a change in the drag force and in the other forces involved in the momentum balance and, thus, causes a change in the overall flow field.

The most common approach to solving eq 16 is to divide the continuous variable L into a finite number of classes or bins, N_c, where the bubble size of the ith class is given by L_i, $i \in 1, \ldots, N_c$. The number density function at L_i is defined as $N_i(\mathbf{x},t) = \int_{L_i}^{L_{i+1}} n(L_i;\mathbf{x},t)\,\mathrm{d}L$. It is useful to recall here that the formulations in terms of bubble size and bubble volume are identical because bubbles are assumed to be spherical. Equation 16 can thus be written as

$$\frac{\partial}{\partial t}[\rho_g N_i(\mathbf{x},t)] + \nabla\cdot[\rho_g N_i(\mathbf{x},t)\vec{v}_g)] = \rho_g[B_i^c(\mathbf{x},t) - D_i^c(\mathbf{x},t) + B_i^b(\mathbf{x},t) - D_i^b(\mathbf{x},t)], \quad i \in 1, \ldots, N_c \tag{23}$$

where the birth and death terms due to coalescence and breakup are approximated by the terms denoted by the i subscript, as will be clearer later. Notice that eq 23 is written in terms of the density ρ_g and the velocity $\vec{v}_g$ of the gas phase.

Several discretization schemes exist for the internal coordinate, and a comparison between different approaches was made by Vanni.[15] A simple approach is to divide the dispersed phase into classes such that the volume of each class is exactly twice as large as the volume of the preceding class.[16,17] It is easy to show that the volume of a bubble belonging to the ith class is

$$v_i = 2^{i-1}v_1 \tag{24}$$

where v_1 is the smallest bubble class considered and $v_i = \pi/6L_i^3$.

An alternative approach to solving eq 16 is the method of moments. This approach is based on the solution of the transport equation of the moments of the bubble size distribution rather than the number density itself. The kth moment is defined as

$$m_k(\mathbf{x},t) = \int_0^\infty n(L;\mathbf{x},t)L^k\,\mathrm{d}L \tag{25}$$

and the transport equation for the kth moment is

$$\frac{\partial}{\partial t}[\rho_g m_k(\mathbf{x},t)] + \nabla\cdot[\rho_g m_k(\mathbf{x},t)\vec{v}_g)] = \rho_g[\bar{B}_k^c(\mathbf{x},t) - \bar{D}_k^c(\mathbf{x},t) + \bar{B}_k^b(\mathbf{x},t) - \bar{D}_k^b(\mathbf{x},t)] \tag{26}$$

and $\bar{B}_k^c(\mathbf{x},t)$, $\bar{D}_k^c(\mathbf{x},t)$, $\bar{B}_k^b(\mathbf{x},t)$, and $\bar{D}_k^b(\mathbf{x},t)$ are the moment transforms of the source terms due to coalescence and breakup and can be expressed as follows

$$\bar{B}_k^c(\mathbf{x},t) = \frac{1}{2}\int_0^\infty n(\lambda;\mathbf{x},t)\int_0^\infty \beta(u,\lambda)(u^3+\lambda^3)^{k/3}n(u;\mathbf{x},t)\,\mathrm{d}u\,\mathrm{d}\lambda \tag{27}$$

$$\bar{D}_k^c(\mathbf{x},t) = \int_0^\infty L^k n(L;\mathbf{x},t)\int_0^\infty \beta(L,\lambda)\,n(\lambda;\mathbf{x},t)\,\mathrm{d}\lambda\,\mathrm{d}L \tag{28}$$

$$\bar{B}_k^b(\mathbf{x},t) = \int_0^\infty L^k\int_0^\infty a(\lambda)\,b(L|\lambda)\,n(\lambda;\mathbf{x},t)\,\mathrm{d}\lambda\,\mathrm{d}L \tag{29}$$

$$\bar{D}_k^b(\mathbf{x},t) = \int_0^\infty L^k a(L)\,n(L;\mathbf{x},t)\,\mathrm{d}L \tag{30}$$

Derivation of the last three terms is trivial, whereas the first term can be derived by using the variable $u^3 = L^3 - \lambda^3$ and substituting $\mathrm{d}L = u^2/L^2\,\mathrm{d}u$.

The main problem in the method of moments is in the closure of eq 26. The RHS of eq 26 can be expressed in terms of lower-order moments only for constant or simple linear forms of the aggregation kernel. An overview of the methods available has been recently published.[18] This limitation is overcome in the quadra-

ture method of moments,[19−23] where the source terms are closed by using a quadrature approximation.

The quadrature approximation is based on determining a sequence of polynomials orthogonal to $n(L)$ (i.e., the bubble size distribution). If the abscissas of the quadrature approximation are the nodes of the polynomial of order N, the quadrature approximation

$$\int_0^\infty f(L)\, n(L)\, \mathrm{d}L \approx \sum_{i=1}^{N} f(L_i) w_i \tag{31}$$

is exact if $f(L)$ is a polynomial of order N or smaller.[24] In all other cases, the approximation is the more accurate the closer $f(L)$ is to a polynomial. A direct way to calculate the quadrature approximation is by means of its definition through the moments

$$m_k = \sum_{i=1}^{N} w_i\, L_i^{\,k} \tag{32}$$

In fact, the quadrature approximation of order N is defined by its N weights w_i and N abscissas L_i and can be calculated by its first $2N$ moments $m_0, ..., m_{2N-1}$. This nonlinear system can be solved by using the Newton−Raphson method or any other nonlinear equation solver. This, however, is not the best approach as a very good initial guess is usually required. A more efficient approach is to write the recursive relationship for the polynomials in terms of the moments m_k. Once this relationship is written in matrix form, it is easy to show that the roots of the polynomials correspond to the eigenvalues of the so-called Jacobi matrix (see algorithm gaucof in ref 25). This is the procedure used in the product−difference (PD) algorithm that was found to be stable in all the tested cases.[26] Once the weights and abscissas are known, the source terms due to coalescence and breakup can be calculated, and therefore, the transport equations for the moments can be solved.

3. Bubble Coalescence and Breakup Kernels

It was noted in the previous section that important pieces of information are contained in the quantities $\beta(L,\lambda)$, $a(L)$, and $b(L|\lambda)$. It was also pointed out that, in the case where bubbles are assumed to be spherical, the formulations in terms of particle length are particle volume are perfectly equivalent

$$a'(v) = a'(L^3) = a(L) \tag{33}$$

and

$$\beta'(v,\epsilon) = \beta'(L^3,\lambda^3) = \beta(L,\lambda) \tag{34}$$

where v is the volume of a bubble of size L and ϵ is the volume of a bubble of size λ. The daughter distribution function instead can be written as

$$b'(v|\epsilon) = \frac{b'(L^3|\lambda^3)}{3L^2} = \frac{b(L|\lambda)}{3L^2} \tag{35}$$

The quantity $\beta(L,\lambda)$ defines the frequency of collisions per unit volume and per unit time of two bubbles of size L and λ that leads to the formation of a new bubble. This can be expressed as the product of two terms,[27] the collision frequency

$$\omega(L,\lambda) = \frac{\pi}{4}(L^2 + \lambda^2)\bar{u}(L,\lambda) \tag{36}$$

and collision probability

$$P(L,\lambda) = \exp\left\{-c_1 \frac{[0.75(1+\zeta^2)(1+\zeta^3)]^{1/2}}{(\rho_g/\rho_l + \gamma)^{1/2}(1+\zeta)^3} We^{1/2}\right\} \tag{37}$$

where c_1 is an unknown constant of order unity that has to be adjusted; ζ is the bubble size ratio L/λ; We is the Weber group, defined as

$$We = \frac{\rho_l L[\bar{u}(L,\lambda)]^2}{\sigma} \tag{38}$$

ρ_l is the density of the liquid phase; ρ_g is the density of the gas phase; and σ is the interfacial tension. $\bar{u}(L,\lambda)$ is the magnitude of the mean gas velocity, calculated as

$$\bar{u}(L,\lambda) = \beta_o^{\,1/2} \epsilon^{1/3} (L^{2/3} + \lambda^{2/3})^{1/3} \tag{39}$$

where ϵ is the turbulent dissipation rate and β_o is a numerical constant equal to 2. These quantities can be derived by applying the kinetic gas theory to the collisions between gas bubbles. For details, one can see ref 27.

The theory related to bubble breakup is not as developed as the theory of coalescence. As for coalescence, one of the main hypotheses is the binary nature of the phenomenon. Two bubbles coalesce to form a larger bubble, and a single bubble breaks up to form two smaller bubbles. The expressions used in this work are based on a theoretical model for drop and bubble breakup in turbulent flows.[28] To make the problem tractable, the turbulence is assumed to be isotropic, and only binary breakage is considered. The turbulent breakage is induced by fluctuating eddies bombarding the bubble surface causing oscillation of the shape of the bubble around its equilibrium shape. Fragmentation occurs if the turbulent motion has enough energy to overcome the increase in surface energy.

In the expression for the daughter distribution function, the breakage volume fraction f_v is assumed to be a stochastic variable with a uniform distribution. For binary breakage, this variable is defined as the ratio of one of the daughter bubble volumes to the parent bubble volume. The breakup function is symmetric about $f_v = 0.5$ for binary breakage. The occurrence of breakage is determined by the energy level of the arriving eddy, and only eddies of length scale smaller than or equal to the particle diameter can induce particle oscillations. The final expression for the breakage kernel is given in the form[28]

$$a'(v)\, b'(\epsilon|v)\epsilon = \Omega_B(v|f_v v) \tag{40}$$

where v is the volume of the parent bubble and ϵ and $v - \epsilon$ are the volumes of the daughter bubbles. In this notation, $\Omega_B(v|f_v v)$ represents the frequency of disrup-

tion of a bubble of volume v forming two daughters of size $f_v v$ and $(1 - f_v)v$ and can be written as

$$\Omega_B(v|f_v v) = c_4\left(\frac{\epsilon}{L^2}\right)\int_{\xi_{min}}^{1}\frac{(1+\xi)^2}{\xi^{11/3}}\exp\left[-\frac{12c_f(f_v)\sigma}{\beta\rho_1\epsilon^{2/3}L^{5/3}\xi^{11/3}}\right]d\xi \quad (41)$$

where L is the size of the bubble of volume v, $c_4 \approx 0.923$, ξ is the ratio between the characteristic size of an eddy l and the bubble size L, and c_f is the coefficient of surface area, defined as

$$c_f(f_v) = f_v^{2/3} + (1 - f_v)^{2/3} - 1 \quad (42)$$

The reported expression for $\Omega_B(v|f_v v)$ takes into account the contributions of all the eddies with characteristic dimension ratios between ξ_{min} and 1; however, according to ref 29, at high Reynolds number

$$\xi_{min} = \frac{l_{min}}{L} \approx 0 \quad (43)$$

The total breakup rate can be computed by integration over f_v as follows

$$a(L) = a'(v) = \Omega_B(v) = \frac{1}{2}\int_0^1 \Omega_B(v|f_v v)\, df_v \quad (44)$$

where the factor $^1/_2$ is due to the fact that the integrand is a symmetric function with respect to $f_v = 0.5$. It is worth noting here that, although the daughter distribution function is not explicity given in the above function, it can be recovered easily from the expression for Ω_B.

4. Solution of the Equations

The following sections illustrate a few specific points about the solution methods used for the CM and QMOM, respectively.

4.1. Classes Method. As mentioned previously, the approach used in this work is based on the gemoetric discretization with ratio 2 proposed by Hounslow.[16] Any coalescence and/or breakup event involves the migration of particles from a given class to the neighboring classes. A particle created through these processes, therefore, can generally fall between two adjacent discrete classes. In such an event, the particles are distributed to the adjacent classes preserving both number and mass. Therefore if a particle of volume v is formed, we assign this particle to the two immediate neighbors, v_i and v_{i+1}, according to $\gamma_i(v){v_i}^r + \gamma_{i+1}(v){v_{i+1}}^r = v^r$, with $r = 0$ and $r = 1$ (conservation of number and mass, respectively) yielding γ_i and γ_{i+1}.

The breakup death rate can be written as

$$D_i^b(\mathbf{x},t) = \sum_{j=1}^{i-1}\Omega_B(v_i,v_j)\, N_j(\mathbf{x},t), \quad i \in 2, ..., N_c \quad (45)$$

whereas the breakup birth rate can be written as

$$B_i^b(\mathbf{x},t) = \sum_{j=i+1,i\neq N_c}^{N_c}\Omega_B(v_j,v_i)\, N_j(\mathbf{x},t) + \sum_{j=1,i\neq N_c}^{i} x_{i+1,j}^b\, \Omega_B(v_{i+1}, v_j)N_j(\mathbf{x},t) + \sum_{j=1,i\neq N_j}^{i-1}(1 - x_{i,j}^b)\Omega_B(v_i,v_j)\, N_j(\mathbf{x},t), \quad i \in 1, ..., N_c \quad (46)$$

where $x_{i,j}^b = 2^{1+j-i}$.

For coalescence, the death and birth terms can be written as

$$D_i^c(\mathbf{x},t) = \sum_{j=1}^{N_c-1}\beta'(v_i,v_j)\, N_i(\mathbf{x},t)\, N_j(\mathbf{x},t) + \beta'(v_i,v_i)\, N_i^2(\mathbf{x},t), \quad i \in 1, ..., N_c - 1 \quad (47)$$

and

$$B_i^c(\mathbf{x},t) = \sum_{j=1,\neq N_c}^{i-1} x_{i,j}^c\beta'(v_j,v_i)\, N_i(\mathbf{x},t)\, N_j(\mathbf{x},t) + \sum_{j=1}^{i-1}(1 - x_{i-1,j}^c)\beta'(v_{i-1},v_j)\, N_{i-1}(\mathbf{x},t)\, N_j(\mathbf{x},t), \quad i \in 1, ..., N_c \quad (48)$$

where $x_{i,j}^c = 1 - 2^{j-i}$.

4.2. Quadrature Method of Moments. The transport equation for the kth moment (see eq 26) can be solved once the mathematical formulations of $\bar{B}_k^c(\mathbf{x},t)$, $\bar{D}_k^c(\mathbf{x},t)$, $\bar{B}_k^b(\mathbf{x},t)$, and $\bar{D}_k^b(\mathbf{x},t)$ are determined. The terms due to coalescence can be written as

$$\bar{B}_k^c(\mathbf{x},t) = \frac{1}{2}\sum_{i=1}^{N} w_i \sum_{j=1}^{N} w_j ({L_i}^3 + {L_j}^3)^{k/3}\beta(L_i,L_j) \quad (49)$$

and

$$\bar{D}_k^c(\mathbf{x},t) = \sum_{i=1}^{N} {L_i}^k\, w_i \sum_{j=1}^{N} w_j\beta(L_i,L_j) \quad (50)$$

where, as already stated, w_i and L_i can be calculated through the PD algorithm starting from the values of the first $2N - 1$ moments $m_k(\mathbf{x},t)$. For the breakage terms, the derivation is somewhat more complicated. According to ref12, the death term can be written as

$$\bar{D}_k^b(\mathbf{x},t) = \sum_{i=1}^{N} w_i {L_i}^k a(L_i) \quad (51)$$

whereas the birth term is

$$\bar{B}_k^b(\mathbf{x},t) = \sum_{i=1}^{N} w_i \int_0^\infty L^k a(L_i)\, b(L|L_i)\, dL \quad (52)$$

Further details on the applications of the QMOM to coalescence and breakage can be found elsewhere.[12]

5. Results and Discussion

The simulations in this paper are based on the air−water system of Hagesather and co-workers.[30] It should

be said that some qualitative and quantitative comparison of model predictions with experimental data were carried out, and preliminarly results showed good agreement. However, as stated in the Introduction, an extensive comparison with experimental data is beyond the scope of this work, and therefore, such results will not be presented. The discussion will, instead, focus on the comparison between two methods (i.e., CM, QMOM) for solving the bubble population balance and their relative costs and accuracies. The column is 4.3 m high and 0.145 m in diameter, of which only 2 m in the axial direction was modeled. The geometry was modeled as being two-dimensional axisymmetric to avoid excessive computational cost. This is a reasonable assumption considering that the focus of this paper is the investigation of different population balance models rather than a detailed study of the hydrodynamics in the column. Time-dependent simulations were run with an average time step of 0.005 s. Initially, the column was assumed to be filled with water, and air bubbles were introduced at the inlet. For the majority of the calculations presented in this paper, the inlet gas velocity was set equal to 0.02 m s^{-1} corresponding to the bubbling regime. Under these operating conditions, quasi-steady state was reached after 20−40 s of real-time simulations. A second set of simulations was carried out at the higher superficial velocity of 0.1 m s^{-1} corresponding to the churn-turbulent case. In this case, quasi-steady state was reached after 80−100 s of real-time simulations.

The breakup and coalescence models used in this paper are strong functions of the turbulent dissipation rate ϵ, which could be calculated by using the mixture turbulence model. However, because of the coarseness of the computational grid and the well-known inability of this model to correctly predict turbulent properties, a constant value of 0.25 m^2 s^{-3} for ϵ was used in all simulations[30] in the bubbling regime. This value is based on the assumption that the average turbulent dissipation in an air−water system is approximately equal to the gas superficial velocity multiplied by the acceleration due to gravity. It is thus clear that this is not an ad hoc value but is based on physical considerations. A detailed exposition is given by Luo.[27]

For purposes of comparison, three different scenarios were studied: (a) no population balance included, (b) population balance modeled using the CM, and (c) population balance modeled using the QMOM. The simulations without the population balance equation were run by setting the mean bubble size equal to the constant inlet value (i.e., $d_{32} = 0.015$ m). In this case, only the Eulerian multiphase equations (i.e., eqs 1 and 2) were solved.

The simulations for the CM were run for four different cases, $N_c = 6$, 12, 18, and 24. As mentioned before, for each case, the volume ratio between successive bubble classes was set equal to 2. For the QMOM simulations, only the first six moments of the bubble size distribution were tracked (i.e., m_0, ..., m_5), which implies the use of a quadrature approximation with three nodes (i.e., $N = 3$). The inlet boundary conditions for the six moments were obtained by calculating the moments of a monomodal distribution centered at 0.015 m.

Figure 1 shows the radially averaged volume fraction of air (gas hold-up) as a function of the axial length. It is clearly seen that, without the population balance equations, the volume fraction of air is almost constant. The small changes are due to the fact that the gas

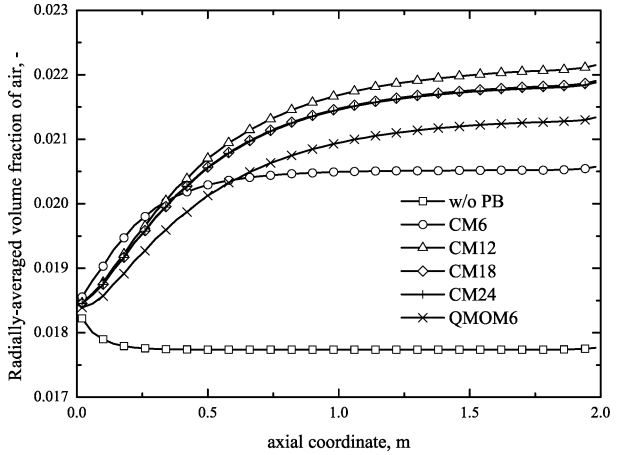

Figure 1. Radially averaged profiles of the gas hold-up versus the axial direction obtained without solution of the population balance, with the CM with 6, 12, 18, and 24 classes and with the QMOM for the low superficial velocity of 0.02 m s^{-1}.

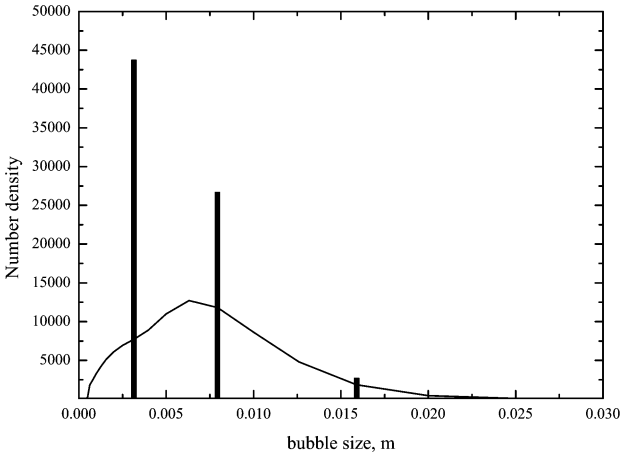

Figure 2. Bubble size distribution for a specific location in the bubble column. Comparison between the CM with 24 classes and the QMOM with six moments. The three nodes are located at their abscissas, and their heights are proportional to their weights.

velocity is not constant throughout the bubble column. Therefore, acceleration or deceleration of the gas phase produces a change in the gas hold-up profile (for conservation of gas mass flux). The introduction of the population balance causes this profile to change radically. By using the CM with six classes, the gas hold-up increases and then reaches a plateau. Essentially, the breakup and coalescence processes dominate near the distributor plate and eventually reach equilibrium further downstream. Doubling the number of classes further from 6 to 12 produces a signinificantly different distribution. However, further refinement of classes to 18 and subsequently 24 seems to produce a solution that is independent of the resolution of the internal coordinate (i.e., bubble classes).

Figure 2 shows the bubble size distribution (i.e., number density as a function of size) for 24 classes at an axial distance of 1.75 m. The number density shown in this plot represents N_i (m^{-3}), which is equal to $\int_{v_i}^{v_{i+1}} n(v)\,dv$, where $n(v)$ (m^{-6}) is the volume-based number density function. The results obtained from the QMOM implemented by using three nodes (and therefore tracking the first six moments) compare favorably with those predicted by the CM. In Figure 2, the position in the bubble size space of the three nodes (i.e., abscissas) is reported, showing that the width of the distribu-

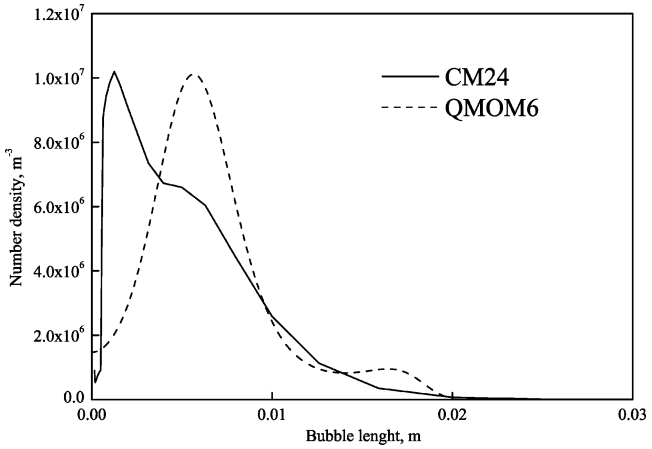

Figure 3. Bubble size distribution for a specific location in the bubble column. Comparison between the CM with 24 classes and the distribution recontructed from the first six moments.

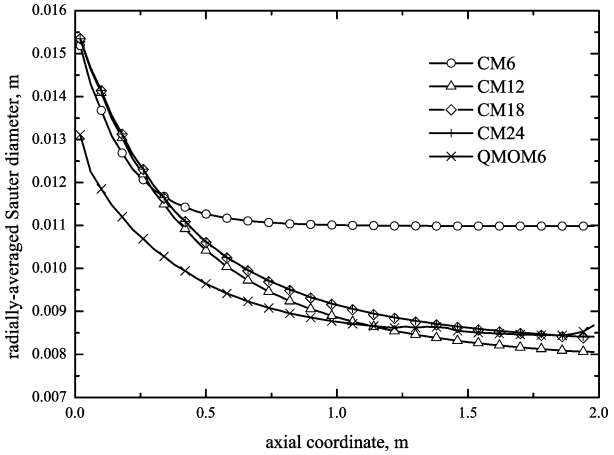

Figure 4. Radially averaged Sauter diameter profiles (d_{32}) versus the axial direction obtained with the CM with 6, 12, 18, and 24 classes and with the QMOM for the low superficial velocity of 0.02 m s^{-1}.

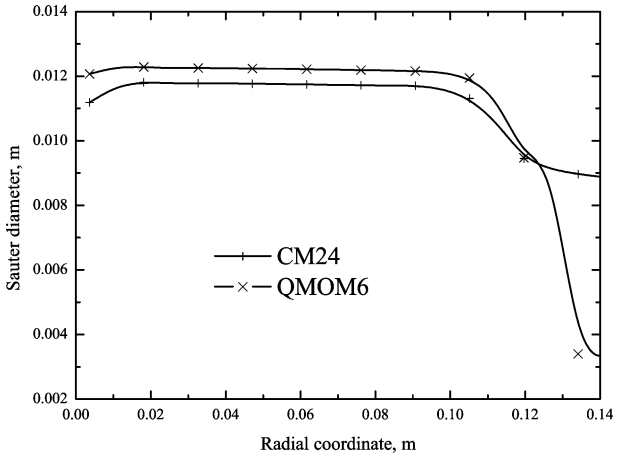

Figure 5. Radial profiles for Sauter diameter (d_{32}) predicted using the CM with 24 classes and the QMOM with six classes at a specific axial position (x = 0.5 m) for the low superficial velocity of 0.02 m s^{-1}.

tion is well captured. It is important to note here, however, that although the three nodes have a purely mathematical connotation, being the abscissas of a quadrature approximation, they can be thought of as three bubble classes with characteristic sizes that actually represent the distribution. Moreover, the mean bubble size, calculated as the ratio of two moments (i.e., $d_{32} = m_3/m_2$), is tracked with the QMOM with higher accuracy than the CM used for the comparison in this work.[12] It is also important to note that the mean bubble size is the only parameter involved in the two-way coupling between flow field calculations and the solution of the population balance.

Starting from the moments of the distribution, it is also possible to solve the inverse problem of reconstructing the bubble size distribution. The number density function, $n(L)$, can be expressed as

$$n(L) = \exp\left(\sum_{i=0}^{N-1} A_i L^i\right) \tag{53}$$

where the coefficients A_i can be determined from the lower-order moments. The method is based on the statistically most probable distribution and was subsequently adapted for crystallization problems.[31] The results from the reconstruction are shown in Figure 3. The plot shows a comparison of the number density function $n(L)$ computed from the CM (24 classes) and that computed from the moments obtained from the QMOM. It is evident that both methods are able to capture the monomodal distribution reasonably well.

In Figure 4, the radially averaged Sauter diameter profiles are plotted as a function of the axial length for the CM with 6, 12, 18, and 24 classes and with the QMOM tracking six moments. It is evident that using only six classes overestimates the Sauter diameter. Increasing the number of classes to 24 or using the QMOM with six moments, however, it becomes possible to predict the final value for the Sauter diameter of about 0.0085 m. It should be highligthed here that the differences between the CM and QMOM near the inlet are caused by the slightly different numerical implementation in the CFD code. In Figure 5, the radial profiles for the Sauter diameter at a specific axial position (x = 1.75 m) predicted by using the CM with 24 classes and the QMOM with six moments are shown. It is observed that the agreement is good. Furthermore, this is also consistent with the fact that bubbles of larger diameters rise through the center of the column whereas the smaller bubbles tend to follow the recirculatory flow along the walls.

In Figure 6, the radially averaged profiles for the bubble number density are reported. Again, using only six classes seems to be inadequate. Only by using 12 classes or more do the model predictions seem to be independent of the number of classes. Also, in this case, the difference in results between the QMOM with six moments and the CM with 18 classes is higher relative to Sauter diameter. This can be attributed to the fact that small differences in the accuracy of the methods cause a large change in the final bubble number density, especially when smaller bubble groups are successively included. However, this does not significantly change the mean bubble size because the small bubbles have a small volume. Thus, although they represent a large part of the population in terms of their number, they represent a very small fraction of the total volume (and therefore are not important for the calculation of the mean bubble size).

Also, for radial profiles of total bubble number density (see Figure 7), the difference between the CM with 24 classes and the QMOM tracking the first six moments is slightly higher than for the other properties. It can

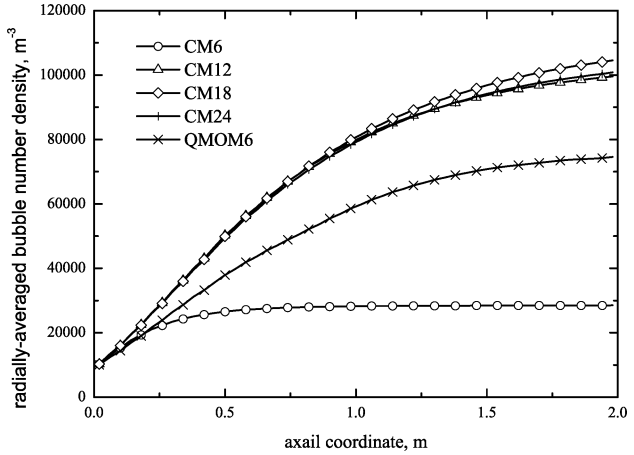

Figure 6. Radially averaged bubble number density (m_0) versus the axial direction obtained with the CM with 6, 12, 18 and 24 classes and with the QMOM for the low superficial velocity of 0.02 m s^{-1}.

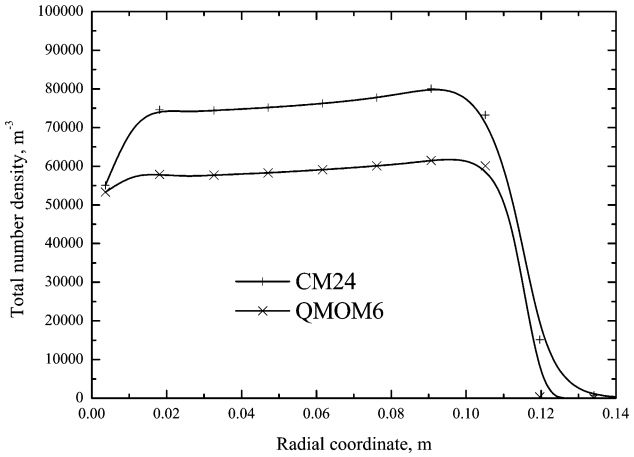

Figure 7. Radial profiles for total number bubble density (m_0) predicted using the CM with 24 classes and the QMOM with six classes at a specific axial position ($x = 0.5$ m) for the low superficial velocity of 0.02 m s^{-1}.

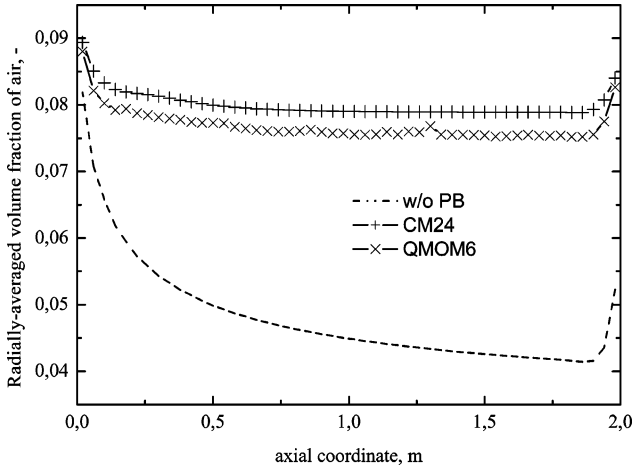

Figure 8. Radially averaged profiles of the gas hold-up versus the axial direction obtained without solution of the population balance, with the CM with 24 classes and with the QMOM for the high superficial velocity of 0.1 m s^{-1}.

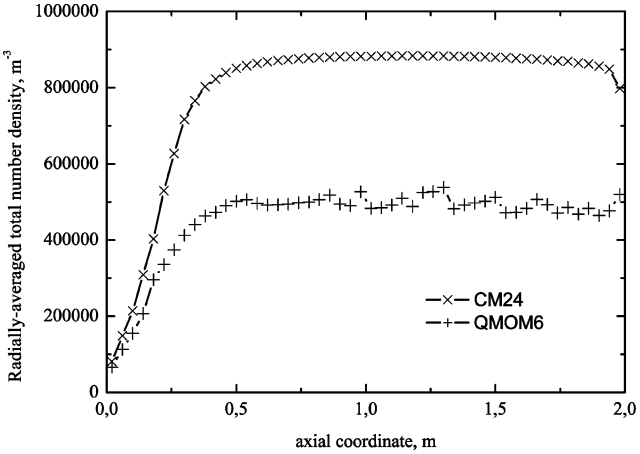

Figure 9. Radially averaged profiles of the total number bubble density m_0 versus the axial direction obtained with the CM with 24 classes and with the QMOM for the high superficial velocity of 0.1 m s^{-1}.

be also be seen that, consistent with decreasing bubble size, the total number density increases radially outward.

All of the above simulations were run in the bubbling regime, where individual bubble shapes can be clearly distinguished. However, as the superficial velocity of the incoming gas is increased, the flow transitions from bubbling to the churn-turbulent regime. The breakup and coalescence processes are much more dominant in this regime. To investigate the effect of including population balance models in this regime, one more set of simulations was performed in which the inlet velocity was increased to 0.1 m s^{-1}. The value of ϵ in the column was appropriately scaled to account for the higher inlet velocity.

Figure 8 shows the radially averaged air volume fraction as a function of axial length. The higher inlet velocity clearly results in a higher overall gas hold-up in this domain compared to the low-inlet-velocity case. Furthermore, the effect of including breakup and coalescence is much more pronounced for the high-velocity case in relation to the low-velocity case. The overall gas hold-up prediction is seen to improve significantly as a result of including the population balance models for the high-velocity case (churn-turbulent regime). By comparison, this effect is much less noticeable for the low-velocity case (bubbling regime).

Figure 9 shows the radially averaged total number density as a function of axial length for the high-velocity case. Consistent with the increased value of turbulence dissipation, the numbers are seen to be an order of magnitude higher than those the low-velocity cases. The general trend, however, is similar to that of the low-velocity cases in that the breakup and coalescence processes tend to negate each other further downstream of the inlet and the plots reach a plateau. The slight oscillations seen in the QMOM simulations are due to instantaneous fluctuations in the near-wall region.

Figure 10 shows the radially averaged Sauter diameter as a function of the axial length for the high-velocity case. The breakup processes clearly dominate near the inlet, leading to a rapid reduction in the mean diameter, eventually reaching a constant value.

6. Conclusions

In this work, bubble column simulations were run coupling the solution of the population balance equation using a CM with 6, 12, 18, and 24 classes and using the QMOM with six moments. Results show that, even

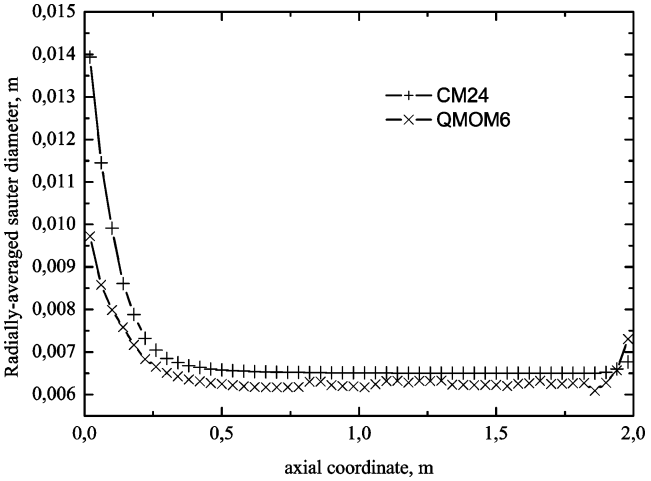

Figure 10. Radially averaged profiles of the Sauter diameter (d_{32}) versus the axial direction obtained with the CM with 24 classes and with the QMOM for the high superficial velocity of 0.1 m s^{-1}.

for low gas velocity, the bubble size distribution changes as a result of coalescence and breakup and, therefore, the solution of the population balance equation is needed. Moreover, the results indicate that, for the CM, the solution is independent of the resolution of the internal coordinate only when the number of classes is greater than 12. This implies that at least 12−18 classes are required to accurately model the entire range of bubble diameters in a typical bubble column.

In contrast, for the QMOM, use of six moments suffices to accurately describe the evolution of the gas phase. In fact, the results found by using the CM with 12 and 16 classes and the QMOM with six moments are very similar. Therefore, use of the QMOM seems to be extremely convenient because it reduces the number of scalars to be used to six without affecting the accuracy of the calculations. It should be recalled here that the two methods are equally stiff, meaning that the CPU times required per scalar solved are about the same.[21] It is therefore clear that, because the QMOM requires fewer scalars, the CPU time for the QMOM is lower than that for the CM. The main disadvantage of the QMOM is the fact that only the moments of the bubble size distribution are known; however, in cases of practical interest when knowledge of the distribution itself is required, one can retrieve the distribution from a finite set of moments.

Finally, although direct experimental results were not presented as part of this paper, the results obtained from the base case (six bubble classes, low gas velocity) compared very well with the numerical and experimental results of Hagesather et al.[30] Furthermor,e extensive calculations for a three-dimensional case have been performed[32] for a cylindrical bubble column, and excellent agreement was reported between the current CFD model and experimental data.

Acknowledgment

This work was financially supported by the U.S. Department of Energy (Project Award DE-FC07-01-ID14087).

Literature Cited

(1) Monahan, S.; Fox, R. O. Effect of grid resolution and force models on flow structures in bubble column simulations. In *8th International Conference Multiphase Flow in Industrial Plants*; ANIMP: Milan, Italy, 2002; pp 69−85.

(2) Sato, Y.; Sadatomi, M.; Segouchi, K. Momentum and heat transfer in two-phase bubble flow. *Int. J. Multiphase Flow* **1981**, *7*, 167.

(3) Sanyal, J.; Vasquez, S.; Roy, S.; Dudukovic, M. P. Numerical simulation of gas−liquid dynamics in cylindrical bubble columns reactors. *Chem. Eng. Sci.* **1999**, *54*, 5071.

(4) Bertola, F.; Vanni, M.; Baldi, G. Application of Computational Fluid Dynamics to Multiphase Flow in Bubble Columns. *Int. J. Chem. React. Eng.* **2003**, *1*, A3.

(5) Sokolichin, A.; Eigenberger, G.; Lapin, A.; Lubbert, A. Dynamic numerical symulation of gas−liquid two-phase flow: Euler/Euler versus Euler/Lagrange. *Chem. Eng. Sci.* **1997**, *52*, 611.

(6) Delnoij, E.; Kuipers, J. A. M.; van Swaaij, W. P. M. Computational fluid dynamics applied to gas−liquid contactors. *Chem. Eng. Sci.* **1997**, *52*, 3623.

(7) Michele, V.; Hempel, D. C. Liquid flow and phase holdup−Measurement and CFD modeling for two-and three-phase bubble columns. *Chem. Eng. Sci.* **2002**, *57*, 1899.

(8) van Baten, J. M.; Krishna, R. Eulerian simulations for determination of axial dispersion of liquid and gas phases in bubble columns operating in the churn-turbulent regime. *Chem. Eng. Sci.* **2001**, *56*, 503.

(9) van Baten, J. M.; Krishna, R. Scale up studies on partitioned bubble column reactors with the aid of CFD simulations. *Catal. Today* **2003**, *79−80*, 219.

(10) Lehr, F.; Millies, M.; Mewes, D. Bubble-size distributions and flow fields in bubble columns. *AIChE J.* **2002**, *48*, 2426.

(11) Marchisio D. L.; Fox, R. O. Solution of population balance equations using the Direct Quadrature Method of Moments. *J. Aerosol Sci.* **2004** accepted.

(12) Marchisio, D. L.; Vigil, R. D.; Fox, R. O. Quadrature method of moments for aggregation−breakage processes. *J. Colloid and Interface Sci.* **2003**, *258*, 322.

(13) Schiller, L.; Naumann, Z. Uber die grundlegenden Berechungen bei der Schwerkraftaufbereitung. *Z. Ver. Dtsch. Ing.* **1935**, *77*, 318.

(14) *Fluent 6.0 User Manual*; Fluent, Inc.: Lebanon, NH, 1999.

(15) Vanni, M. Approximate population balance equations for aggregation−breakage processes. *J. Colloid Interface Sci.* **2000**, *221*, 143.

(16) Hounslow, M. J.; Ryall, R. L.; Marshall, V. R. A discretized population balance for nucleation, growth, and aggregation. *AIChE J.* **1988**, *34*, 1821.

(17) Lister, J. D.; Smith, D. J.; Hounslow, M. J. Adjustable discretized population balance for growth and aggregation. *AIChE J.* **1995**, *41*, 591.

(18) Diemer, R. B.; Olson, J. H. A moment methodology for coalescence and breakage problems: Part I.I Moment models and distribution reconstruction. *Chem. Eng. Sci.* **2002**, *57*, 2211.

(19) McGraw, R. Description of aerosol dynamics by the quadrature method of moments. *Aerosol Sci. Technol.* **1997**, *27*, 255.

(20) Barrett, J. C.; Webb, N. A. A comparison of some approximate methods for solving the aerosol general dynamic equation. *J. Aerosol Sci.* **1998**, *29*, 31.

(21) Marchisio, D. L.; Pikturna, J.; Fox, R. O.; Vigil, R. D.; Barresi, A. A. Quadrature method of moments for population balances. *AIChE J.* **2003**, *49*, 1266.

(22) Rosner, D. E.; Pyykonen, P. P. Bivariate moment simulation of coalescence and sintering nanoparticles in flames. *AIChE J.* **2002**, *48*, 476.

(23) Wright, D. L.; McGraw, R.; Rosner, D. E. Bivariate extension of the quadrature method of moments for modeling simultaneous coalescence and sintering of particle populations. *J. Colloid Interface Sci.* **2001**, *36*, 242.

(24) Dette, H.; Studden, W. J. *The Theory of Canonical Moments with Applications in Statistics, Probability, and Analysis*; John Wiley & Sons: New York, 1997.

(25) Press, W. H.; Teukolsky, S. A.; Vetterling, W. T.; Flannery, B. P. *Numerical Recipes in C: The Art of Scientific Computing*, 2nd ed.; Cambridge University Press: Cambridge, U.K., 1992.

(26) Gordon, R. G. Error bounds in equilibrium statistical mechanics. *J. Math. Phys.* **1968**, *9*, 655.

(27) Luo, H. Coalescence, breakup and liquid circulation in bubble column reactors. Dr. Ing. Thesis, University of Trondheim, Trondheim, Norway, 1993.

(28) Luo, H.; Svendsen, H. F. Theoretical model for drop and bubble breakup in turbulent dispersions. *AIChE J.* **1996**, *42*, 1225.

(29) Tennekes, H.; Lumley, J. L. *A First Course on Turbulence*; The MIT Press: Cambridge, MA, 1972.

(30) Hagesather, L.; Jakobsen, H.; Svendson, H. A Coalescence and Breakup Module for Implementation in CFD Codes. In *10th European Symposium on Computer Aided Process Engineering, ESCAPE 10*; Elsevier: Amsterdam, 2000; p 367.

(31) Baldyga, J.; Orciuch, W. Barium Sulphate Precipitation in a Pipe—An Experimental Study and CFD Modeling. *Chem. Eng. Sci.* **1999**, *56*, 2435.

(32) Chen, P.; Sanyal, J.; Dudukovic, M. P. Three Dimensional Simulation of Bubble Column Flows with Bubble Coalescence and Breakup. Accepted for publication in *AIChE*.

Received for review May 24, 2004
Revised manuscript received July 28, 2004
Accepted August 6, 2004

IE049555J